Advances in Microstructural Understanding of Wrought Aluminum Alloys

J.D. ROBSON, O. ENGLER, C. SIGLI, A. DESCHAMPS, and W.J. POOLE

Wrought aluminum alloys are an attractive option in the quest for lightweight, recyclable, structural materials. Modern wrought aluminum alloys depend on control of complex microstructures to obtain their properties. This requires an understanding of the coupling between alloy composition, processing, and microstructure. This paper summarizes recent work to understand microstructural evolution in such alloys, utilizing the advanced characterization techniques now available such as atom probe tomography, high-resolution electron microscopy, and synchrotron X-ray diffraction and scattering. New insights into precipitation processes, deformation behavior, and texture evolution are discussed. Recent progress in predicting microstructural evolution using computer modeling is also summarized.

https://doi.org/10.1007/s11661-020-05908-9

I. INTRODUCTION

ALUMINUM and its alloys are second only to steel in usage as engineering metals, with over 64 million tonnes produced in 2018.[1] This usage continues to grow at around 6 pct annually, driven by the increased need for lightweight, strong, corrosion resistant, recyclable, and economic material. Over 80 pct of aluminum is used in wrought products that are produced by thermomechanical processing (including rolling, extrusion, and forging). It is now well understood that the properties of aluminum alloys depend crucially on their microstructure, and that the complex processing a typical wrought alloy experiences profoundly effects this microstructure and hence final properties. Therefore, microstructural understanding is essential to design alloys with improved properties to meet today's demanding challenges in performance and sustainability.

Modern wrought aluminum alloys are sophisticated materials, typically containing at least five deliberate alloying additions and impurity elements (that can themselves be essential), which are subject to complex process pathways. Most of the principles used in modern aluminum alloys were discovered through trial and error, without a mechanistic understanding. A classic example is the accidental discovery of age hardening by Wilm in 1906, the primary strengthening mechanism in modern high strength aluminum alloys.[2] Not until the advent of X-ray characterization some 30 years later could a mechanistic explanation be provided, relating the natural age hardening effect to the formation of small solute enriched regions now referred to as Guinier-Preston (GP) zones.[3,4] It was a further 20 years until these zones could be directly detected in electron microscopy *via* strain contrast[5] and approximately another 40 years until high-resolution electron microscopy was sufficiently advanced to confidently image the atomic structure of the GP zones.[6] By this point, alloys relying on these precipitates for their strength had been in commercial use for over 70 years.

Indeed, over a century of experimentation, alloys and processes have been developed by empirical experimentation that rely on extremely sophisticated microstructural manipulation to obtain the required properties. It has therefore been a major task to understand mechanistically how these materials work, enabling new alloys and processes to be designed based on physical principles.

An improved understanding of microstructural mechanisms is critical to address current challenges in wrought aluminum alloys, for example to enable closed loop recycling, or develop alloys with both high strength and formability. This review is not intended to be

J.D. ROBSON is with the Department of Materials, University of Manchester, Manchester M13 9PL, UK. Contact e-mail: joseph.d.robson@manchester.ac.uk O. ENGLER is with the Hydro Aluminum Rolled Products GmbH, Research and Development Bonn, PO Box 2468, 53014 Bonn, Germany. C. SIGLI is with the Constellium Technology Center, CS 10027, 38341 Voreppe Cedex, France. A. DESCHAMPS is with the Université Grenoble Alpes, CNRS, Grenoble INP, SIMAP, 38000 Grenoble, France. W.J. POOLE is with the Department of Materials Engineering, The University of British Columbia, Vancouver, BC V6T 1Z4, Canada.

Manuscript submitted March 12, 2020.
Article published online July 8, 2020

exhaustive, but instead aims to briefly summarize these latest developments in microstructural understanding and simulation, suggesting avenues for future research.

II. ADVANCES IN CHARACTERIZATION TECHNIQUES

Microstructural understanding of wrought aluminum alloys is intrinsically linked to the characterization techniques available. In classifying characterization techniques, it is useful to make a distinction between global and local methods. Global methods provide spatially averaged microstructural information for the volume of material being investigated, usually by a measurement that is related to a microstructural feature (or combination of features). Common techniques that are widely used in this class include hardness, electrical conductivity (EC), thermo-electric power (TEP), differential scanning calorimetry (DSC), X-ray diffraction (XRD), and small angle scattering of X-rays or neutrons (SAXS and SANS respectively[7]).

Local methods provide spatially resolved information that reveal not only the nature of the microstructural feature but also its location. Examples include optical microscopy (OM), electron microscopy (scanning and transmission, SEM and TEM respectively), atom probe tomography (of which there are several types[8]), and electron backscattered diffraction (EBSD). These classes of techniques are complementary, and understanding is often maximized by employing a combination of methods to obtain both global and local information about the microstructure.

There are two aspects of wrought aluminum alloy microstructures that are usually dominant in controlling properties and are therefore usually the focus of characterization efforts. In age hardenable alloys, the formation and distribution of second-phase precipitates is the critical issue. In non-age hardenable alloys, grain structure and texture tend to be of greatest importance.

The challenge in studying precipitation in aluminum alloys is that the microstructural features of interest are very small; on the sub-nanometer scale in the case of GP zones. Furthermore, the initial clustering and nucleation process that leads to the first precipitates can be very sensitive to minor alloying elements or availability of excess vacancies.[9,10] This requires coupling of techniques with atomic resolution with other techniques capable of studying representative volumes of material.

A particularly powerful combination of techniques to gain new insights into precipitation processes involves using atom probe to study the initial clustering processes, high-resolution electron microscopy (HREM) to study the evolving precipitates at a local scale and SAXS to provide global information. By using compositionally graded or tapered specimens, it is possible to use high speed SAXS to simultaneously track, *in situ*, the precipitation kinetics as a function of composition or applied strain, collapsing a large experimental matrix into a single specimen.[11,12] An example of a combination of SAXS and HREM applied to understand precipitation in Al-Cu-Li-X alloys is shown in Figure 1.[13–15] In this case, SAXS can provide only a relative volume fraction, but this was related to the actual volume fraction using DSC. The assumption of a platelet morphology permits the precipitate thickness to be determined from the radially averaged SAXS intensity; full details given elsewhere.[15]

III. PRECIPITATION

Pure aluminum is too weak for structural applications and thus strengthening is essential. Unlike other metals (such as ferrous alloys), there is no allotropic phase transformation in aluminum that can be exploited to provide strengthening through structural refinement. Wrought Al alloys are commonly subdivided into two classes, heat treatable and non-heat treatable alloys, depending on their main hardening and strengthening mechanism. Alloys of the AA 2xxx, 6xxx, and 7xxx series are heat treatable, *i.e.*, they may be strengthened by controlled heating and quenching sequences followed by natural or artificial aging to form strengthening precipitates. In contrast, the strength of the so-called non-heat treatable alloys of the AA 1xxx, 3xxx, and 5xxx series is provided by a combination of solid-solution hardening and dispersion hardening of their main alloying elements (Section IV).

The most remarkable improvements in strength are obtained through the formation of second-phase precipitates. Strong, precipitation strengthened aluminum alloys can achieve yield stress values approaching 100 times that of pure aluminum. Since the strengthening effect depends strongly on the precipitate size, shape, spacing, and distribution, an understanding of these parameters for the different classes of aluminum alloys is critical to optimize performance.

A. *Al-Cu-Mg (Ag, Li) 2xxx Alloys*

The Al-Cu binary system is the prototype for age hardening in aluminum and has thus been extensively studied for decades. Even this binary system is complex, and new details of the precipitate structures are still being uncovered.[16]

The Al-Cu-Mg system forms the basis of most commercial 2xxx alloys, which were the first widely used precipitate strengthened (age hardened) aluminum alloys. The precipitation sequences in these alloys are different depending on the Mg:Cu ratio and are also altered by the addition of Li or small amounts of Ag.[17]

Atom probe and HREM have provided new insights into the initial clustering processes that precede precipitate formation, and the internal structure of precipitate particles. For example, the powerful effect that small additions of Ag have in changing the precipitation sequence in Cu-rich Al-Cu-Mg alloys from θ (and its precursors) to Ω has been demonstrated to be due to clustering of Ag and Mg in the first steps of precipitation, as detected by atom probe.[18] This has important effects on the mechanical properties, since the Ω plates have a {111} rather than {100} habit plane, which changes their interaction with dislocations. The

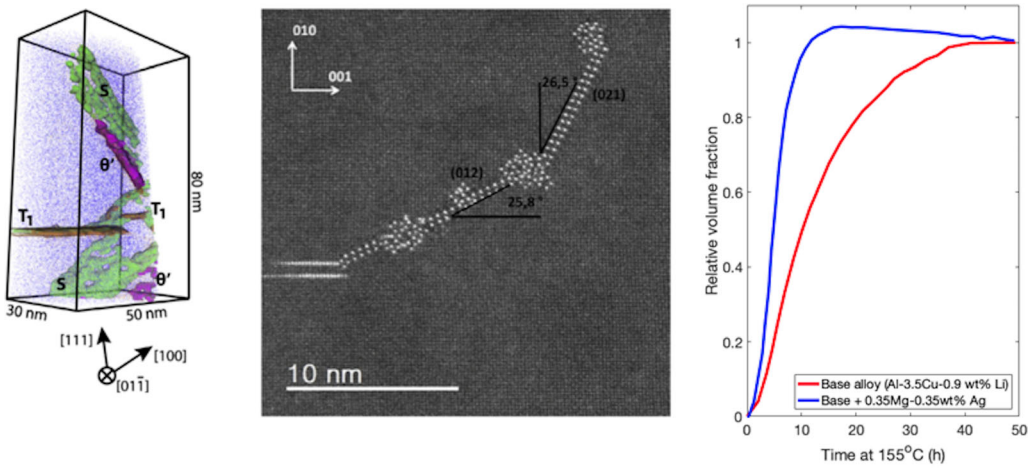

Fig. 1—Multi-scale characterization of precipitation in Al-Cu-Mg-Li. (*a*) Atom probe analysis showing precipitate composition and 3-dimensional morphology. (*b*) HREM imaging of the precipitate structures. (*c*) Evolution of average precipitate size and volume fraction determined by SAXS. Figures reproduced from Refs. [13]–[15] with permission from Elsevier. *Note* (a, b) are different alloys at different stages of ageing.

segregation of Mg and Ag to the interface of the Ω precipitates, as determined by HREM, also explains the improved coarsening resistance of these Ω precipitates.[19]

Third generation Al-Li alloys (Al-Cu-Mg-Li) present complex microstructures where a number of different precipitation sequences can be observed simultaneously, depending on alloy composition. In alloys with relatively high Li content (such as AA2196) precipitates of δ' (Al_3Li), θ' (Al_2Cu) and T_1 (Al_2CuLi) can be observed after industrial age hardening, each competing for solute. In lower Li content alloys (*e.g.*, AA2198), subject to predeformation, the T_1 (Al_2CuLi) phase is dominant.[17]

The T_1 phase has interesting characteristics in both its formation and strengthening mechanism. It is difficult to nucleate this phase homogeneously, but the introduction of dislocations greatly enhances its formation by providing heterogeneous nucleation sites, thought to be associated with stacking fault between partial dislocations.[20] T_1 grows as plates on (111) habit planes which lengthen without thickening during growth, leading to platelets that are typically 100 nm in length but only 1.3 nm thick.[21] The network formed by these platelets provides a formidable obstacle to dislocation motion and therefore highly effective strengthening.

HREM has revealed these precipitates to have a complex layered structure, with a Li-rich central layer bounded by two corrugated Cu-rich layers, with an outer corrugated Al-Cu-Li layer.[22,23] This is important in explaining their deformation behavior. It has been shown that T_1 precipitates are shearable, and usually this would be considered undesirable since it leads to slip localization as subsequent dislocations find it easier to shear the precipitate on the same plane. However, in the case of the T_1 phase, the layered structure means that a 2nd shearing event on the same plane is highly unfavorable, and thus slip localization does not occur.[24] Example images showing T_1 plates that have undergone single shear on multiple planes are presented in Figure 2(a).[24]

B. *Al-Mg-Si-(Cu) 6xxx Alloys*

Detailed research since the 1990s has shown that the precipitation sequence in Al-Mg-Si is much more complicated than originally thought. The advent of high-resolution transmission electron microscopy and 3D atom probe has provided a more detailed description. The generally accepted precipitation sequence in copper free alloys is[25–28]:

Supersaturated solid solution (SSSS)
→ atomic clusters → GP zones
→ metastable β'' phase
→ metastable β', $U1$, $U2$, β' phases
→ stable β phase

The β'' is the main strengthening precipitate for peak aged materials and has an atomic structure characterized by stackings of a specific basic unit usually referred to as a β'' "eye".[29] The atom probe results of Hasting *et al.* suggested that it contains Al, *i.e.*, a stoichiometry of $Mg_5Si_4Al_2$[30] (although this may very well be chemistry dependent). The nature of the dislocation-precipitate interaction is critical for developing quantitative models of strength and work hardening. Recent results from Christiansen *et al.* show direct observations for shearing of β'' at the peak strength.[31]

The quest to produce higher strength 6xxx alloys has led to considerable research on the effect of copper additions. With the addition of copper, precipitation sequence is altered to the following[25,32–38]:

Supersaturated solid solution (SSSS)
→ atomic clusters → GP zones
→ metastable β'', L, C, QP, QC phases
→ metastable β', Q' → stable Q phase

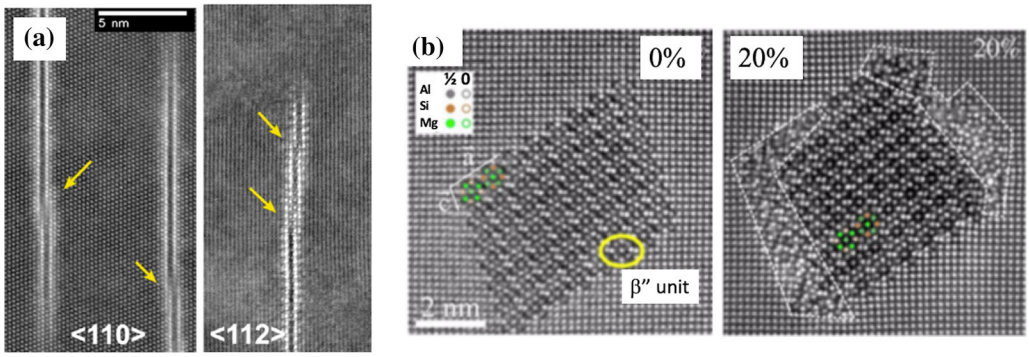

Fig. 2—(*a*) T_1 plates in Al-Cu-Mg-Li alloy showing layered structure and single shearing events on multiple planes.[24] (*b*) Evidence for precipitate shearing in peak aged 6xxx alloy (comparing no-strain and 20 pct strain case, with sheared regions outlined[31]). Figures reproduced from Refs. [24] and [31] with permission from Elsevier.

First principle calculations using density functional theory have emerged as an important modeling tool to predict the crystal structure and thermodynamic properties for metastable precipitates *e.g.*, Reference 39. Microalloying can also influence the precipitation behavior (*e.g.*, Ag effect[40]).

C. *Al-Zn-Mg-(Cu) 7xxx Alloys*

7xxx series alloys contain two families, the Cu free Al-Zn-Mg alloys and the Cu containing Al-Zn-Mg-Cu alloys. It is this latter family that provide the strongest of all aluminum alloys and are thus of great interest in strength limited applications. Traditionally used in aerospace, such alloys are increasingly of interest to the automotive sector due to their lightweighting potential.[41] Maximum strengthening is provided by Mg- and Zn-rich η' precipitates, and increasing strength can be achieved by maximizing the volume fraction of these precipitates by maximizing the alloying content. However, 7xxx alloys can also be susceptible to stress corrosion cracking (SCC), and empirically it has been demonstrated that this places limits on the safe composition space.[42] To combat the SCC issue, high strength 7xxx alloys are also usually used in an overaged temper, which has been demonstrated to improve SCC performance, albeit at a loss of some strength. Many multi-step tempers have been developed in an attempt to achieve both high strength and good SCC resistance.[43]

The relationship between alloy composition, microstructure, and SCC performance is complex.[44] Recent work using atom probe offers new insights by enabling investigation of solute segregation and clustering at the necessary atomic resolution. It has been shown that in the as-quenched state there is an excess of Mg, Zn, and Cu on grain boundaries of about a factor 2-3.[45] The precipitates that form are not stoichiometric compounds, but contain Al, Mg, Zn, and Cu.[45] The precipitates also have a regular layer structure, as demonstrated by HREM analysis.[46] Only on over-aging do the precipitates enrich in Cu (which is the slowest diffuser of the major alloying additions).[47] This may contribute to the improvement in SCC performance.[48]

To meet the increasing demand for 7xxx alloys in the automotive sector, different strategies are required to optimize microstructure due to the requirements for reduced cycle times and high formability.[41] Understanding the coupling between deformation (during forming) and precipitate evolution is also critical (see Section III–F).

D. *$L1_2$ Al_3X Strengthened Alloys*

One important limitation of the precipitation strengthened alloys is that the precipitates are thermally unstable as temperature increases, and their strengthening effect is severely degraded above about 250 °C.[49] In the search for high strength aluminum alloys capable of operating at higher temperatures, alternative systems have been explored in which more stable precipitates form. A candidate precipitation system is found in alloys which form $L1_2$ Al_3X dispersoids.[50] This compound is an ordered form of the face-centered cubic aluminum lattice, precipitating from slow diffusing transition metal additions (X) with a fully coherent interface.[51] A key limitation of these alloys is that the maximum solubility of the transition metals is less than 0.6 at. pct,[52] limiting the maximum supersaturation that can be produced and hence volume fraction of precipitation. However, by combining a cocktail of $L1_2$ forming elements with other additions capable of high temperature strengthening, promising advances have been made towards high strength, high temperature aluminum alloys (*e.g.*, Reference 53).

An important example of a beneficial cocktail effect is the combined addition of Sc and Zr to form $Al_3(Sc,Zr)$ dispersoids. In addition to boosting the volume fraction and compensating for the opposite segregation tendency of these elements,[54] benefit arises from the formation of a core-shell dispersoid structure (Figure 3(b)[55]). Sc, the faster diffusing element, is concentrated in the dispersoid core and Zr, the slower diffuser, in the outer shell.[55,56] This reduces the coarsening rate of the dispersoids, enabling a finer and more effective distribution to be maintained. Modeling can successfully predict the evolution of the core-shell structure and is discussed in Section VI–B.

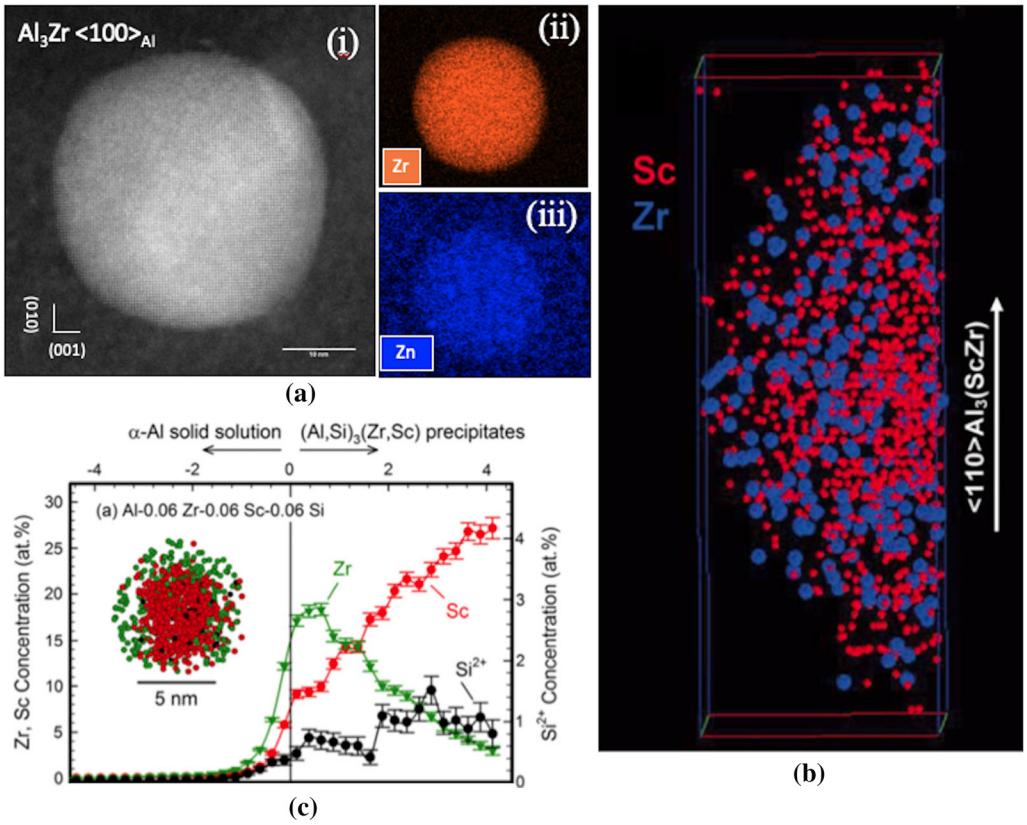

Fig. 3—(*a*)(i) HREM image of a coherent $L1_2$ Al_3Zr dispersoid in an Al-Zn-Mg-Cu alloy showing (ii) Zr and (iii) elevated Zn.[60] (*b*) Atom probe analysis revealing core-shell structure of $L1_2$ $Al_3(Sc,Zr)$ dispersoids, with a Sc-rich core and Zr-rich shell.[55] (*c*) Atom probe analysis revealing core-shell structure and silicon incorporation into $L1_2$ dispersoids (0.06 wt pct Si alloy).[57] Figures reproduced from Refs. [55], [57], [60] with permission from Elsevier.

A large body of work now exists on the $L1_2$ forming aluminum alloys, with many additions explored in addition to Zr and Sc, including Ti, Hf, V, Nb, Ta (slow diffusers), Li, Er, and Mn.[50,53] Most of these additions are designed to substitute onto the (Sc, Zr) sublattice, but some elements can influence $L1_2$ precipitation by substituting onto the Al sublattice. Both Zn (Figure 3(a)) and Si have been demonstrated to have this behavior.[57–60] Si has been shown to strongly accelerate nucleation of the $L1_2$ Al_3X phase, enabling a finer and more effective distribution to be obtained through a shorter heat treatment (Figures 3(b) and (c)[57,61]). The Si effect has been shown by atom probe analysis and atomistic modeling to be consistent with an accelerating effect on initial solute clustering.[57]

E. *Effect of Natural Ageing on Precipitation*

In the presence of excess vacancies after quenching, ambient temperature is sufficient to provide the thermal energy needed to initiate solute clustering and GP zone formation in most precipitate forming aluminum alloys. This leads to the "natural ageing" effect, where the alloy strengthens over time after quenching. The natural ageing process can have a profound effect on subsequent precipitation during heating (artificial ageing), and the nature of this effect depends strongly on the alloy composition.[17] For example, in 6xxx alloys, natural ageing strongly delays subsequent precipitation during heating, especially the for the industrially important paint bake cycle of around 20 minutes at 180 °C. To minimize this effect, one approach for 6xxx alloys is to preanneal the solution-treated material at a temperature in the range of 50 °C to 100 °C, known as preageing or a T4P temper, to stabilize the microstructure.[62,63] Figure 4 shows the beneficial impact of preageing on reducing the time to peak strength for the bake-hardening response of autobody sheet by comparing the evolution of hardness, HV5, during artificial ageing of alloy AA6016 in three different conditions. It is seen that natural ageing for 30 days significantly delays the progress of age hardening; for a typical paint bake cycle of 20 minutes at 185 °C virtually no hardness increase is obtained (T61 temper state). Preageing for 24 hours at 70 °C has a stabilizing effect, in that the ageing proceeds approximately as in the freshly quenched condition.[63]

The clustering of solute at ambient temperature in Al-Mg-Si alloys has received considerable attention in the literature since the advent of 3D atom probe tomography.[26] Most recently, De Geuser and Gault have summarized the ability and limits of cluster characterization by this instrument[64] and some remaining challenges have been discussed by Peng *et al.*[65] Marceau *et al.*[66] rationalized the strengthening effect of clusters based on their size and number density. The

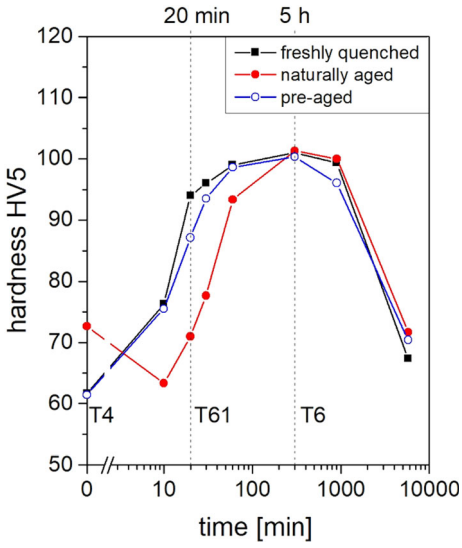

Fig. 4—Evolution of hardness HV5 with ageing time during artificial ageing of alloy AA6016 in various conditions.[63] Figure reproduced from Ref. [63] with permission of Elsevier.

physical basis for the origin of cluster strengthening[67] has been considered in terms of local bond breaking[67] and more recently using molecular dynamics simulations on a model Al-Mg system.[68]

Another very interesting approach to stop or delay the natural ageing of 6xxx is that of microalloying with elements that interact with vacancies. Pogatscher *et al.* have shown that Sn and In can be used to control diffusion at room temperature but have a minimal effect at the artificial ageing temperature (they term this "diffusion on demand"[69,70]).

The effect of natural ageing on the artificial ageing is highly dependent on alloy type. For example, the negative effect described above for 6xxx alloys is opposite to a positive effect seen in 7xxx alloys, where natural aging accelerates artificial ageing kinetics.[17] This difference is important in designing process paths for the different classes of alloys.

F. *Effect of Deformation on Precipitation*

Plastic deformation can profoundly influence precipitation processes in aluminum alloys and this has recently received renewed attention.[71] The nature of the interaction is complex and depends on both the initial state of the alloy (*e.g.*, degree of supersaturation) and the order in which deformation and precipitation occur (*e.g.*, sequentially or simultaneously).[72]

Plastic deformation induces defects into the crystal; most importantly dislocations and deformation induced vacancies. These induced defects influence all aspects of the precipitation process, from nucleation and growth to coarsening.[73] In general, by providing both heterogeneities to assist precipitate nucleation and diffusion enhancement, these defects accelerate the precipitation kinetics.

In the case where the initial condition is supersaturated and precipitation occurs during plastic deformation, it has been shown that there is both enhanced nucleation and growth of precipitates, and the accelerating effect increases with the plastic strain.[11,17,73,74] Furthermore, it has been clearly demonstrated that the dominant kinetic effect arises from the large number of deformation induced transient excess vacancies.[17,73] This can be exploited to form a desirable distribution of small strengthening precipitates by using cyclic deformation.[71]

In the case where precipitation follows deformation, the effect of induced defects can either be positive or negative with regard to ageing response. Industrial sheet and plate processing involves stretching the material prior to ageing. This induces plastic deformation that can be critical in assisting precipitate nucleation.[17] As discussed in previous sections, deformation is necessary for the nucleation of the strengthening T_1 phase in Li containing 2xxx alloys. In contrast, in 7xxx alloys, stretching reduces the age hardening response slightly, and this has been attributed to nucleation of η precipitates on dislocations that remove solute.[75,76] Predeformation can therefore have either a positive or negative effect on precipitation after ageing; in alloys where the precipitates can form readily from precursors within the matrix the effect is negative, but in alloys where dislocations are required to promote precipitate nucleation, the effect is positive.

Finally, the case where deformation occurs after precipitation can be considered. In the case where precipitates are small and shearable, this can lead to dissolution when the sheared precipitates become smaller than the critical size for stability.[77] When the precipitates are large and unsheared, hot or warm deformation can produce a strong accelerating effect on precipitate coarsening of several orders of magnitude, due to both enhanced vacancy concentration and pipe diffusion along dislocations.[78] This can mean that even particles that would usually be considered "stable", such as dispersoids, can evolve rapidly, even during relatively short exposure times.[79]

IV. QUENCHING, CONSTITUENTS, AND DISPERSOIDS

In addition to strengthening precipitates, there are several other classes of particle that can form in aluminum alloys and have a profound effect on properties.

Quench-induced precipitation occurs when cooling rates from solution treatment are insufficiently rapid to prevent nucleation and growth of precipitates at heterogeneous sites such as grain boundaries or dispersoid particles. It is detrimental to subsequent age hardening response and usually undesirable, but may be unavoidable (*e.g.*, in thick sections). The susceptibility of an alloy to quench induced precipitation is defined by its quench sensitivity. Further details are given in a recent review on this topic.[80]

Commercial aluminum alloys always contain Fe as an impurity and often have Mn or Cr added as alloying additions. These transition metals segregate during solidification either by eutectic or peritectic reactions. Segregation and the formation of Fe based intermetallics (known as constituent particles) during typical DC casting processes are reviewed in detail elsewhere.[81] The intermetallic particles typically have dimensions in the order of microns (and are therefore the largest particles in the microstructure). The constituent particles can have beneficial effects, *e.g.*, the control of recrystallization textures in 3xxx alloys by particle stimulated nucleation or negative effects, *e.g.*, the lowering of ductility in 5xxx[82] and 6xxx alloys.[83] In some alloys, *e.g.*, 3xxx, and 6xxx, it is important to design alloy composition and heat treatment to obtain the correct balance of constituent particles. For example, as-cast billets of 6xxx produced by direct chill (DC) casting typically have two types of major Fe bearing constituent particles, α-Al(MnFe)Si and β-AlFeSi.[84] The β-AlFeSi has a plate morphology and has negative effects on hot workability and subsequent room temperature ductility. As such, Mn is often added which promotes the formation of α-Al(MnFe)Si during solidification and also the transformation of β-AlFeSi to α-Al(MnFe)Si during homogenization.[85] The α-Al(MnFe)Si particles have a more spherical shape which is better for high and low temperature ductility. The transformation during homogenization is strongly chemistry dependent[86] and recent work has modeled this process.[87–90]

Dispersoid particles, recently reviewed elsewhere,[91] are commonly used in wrought aluminum alloys to control the grain structure during thermomechanical processing by controlling recrystallization and grain growth. The $L1_2$ Al_3Zr phase already discussed is commonly used for this purpose in modern 7xxx alloys. In other alloy systems, there is often a coupling between dispersoids and strengthening precipitates. For example, in 6xxx alloys there is a particularly complex interaction between Mg-Si precipitates and nucleation of α-AlMnFeSi dispersoids.[92] Models can help understand these interactions.[90]

V. DEFORMATION, RECRYSTALLIZATION, GRAIN GROWTH, AND TEXTURE DEVELOPMENT

Control of grain structure and texture is often critical to the performance of wrought aluminum alloys. The work hardening that accompanies deformation is also an important strengthening mechanism, particularly in the non-age hardenable alloys. In these materials, additional strengthening is often created by cold working, typically using cold rolling, to the strain-hardened tempers H1x. Back annealing at elevated temperatures causes recovery, which is accompanied by a reduction in strength and increase in ductility to the tempers H2x. Annealing at sufficiently high temperatures of typically about 350 °C and higher will give rise to recrystallization, resulting in the fully soft annealed O temper condition which is characterized by maximum formability. Both work hardening and softening of Al alloys is commonly accompanied by the formation of preferred crystallographic orientation, or texture, which typically results in significant plastic anisotropy of Al sheet or profiles. The following section summarizes recent advances in understanding and modeling these processes to enable better prediction of formability and final properties.

A. *Deformed State*

During deformation at ambient temperatures thermally activated processes do not play a significant role, hence plastic behavior is largely independent of the strain rate. Work hardening and microstructure evolution are a consequence of the fact that the stress required for dislocation movement usually increases during plastic flow as the dislocations become increasingly hindered by microstructural obstacles. In order of increasing size these obstacles are solute atoms, dislocations, precipitates and grain boundaries, where the most important variation in obstacle density is due to the dislocations themselves. The dislocation density and distribution evolves with increasing strain, described in detail for aluminum alloys elsewhere.[93]

Deformation at elevated temperature is strongly influenced by thermally activated processes so that the flow stress becomes temperature and strain rate dependent (viscoplastic). The microstructure evolution is mostly controlled by strong dynamic recovery of the dislocation arrangements into a well-defined subgrain structure. The flow stress tends to saturate at a value depending on temperature, strain rate, and alloy content.

The large plastic strains encountered in deformation processes like rolling and extrusion are accompanied by the development of pronounced crystallographic textures, which can strongly influence the resulting mechanical properties of the material. The most well-known effect is the plastic anisotropy of sheet products, including, *e.g.*, the occurrence of earing during a subsequent deep drawing operation (*e.g.*, Reference 94).

B. *Recovery and Recrystallization*

During deformation, dislocations are formed and stored. In the early stages of annealing the material gradually softens, which is caused by recovery reactions. The term recovery combines all dislocation reactions, including dislocation annihilation and rearrangement into more stable cell or subgrain structures. Subsequently, the subgrains may coarsen, thereby reducing the subgrain boundary energy. Despite these obvious microstructural changes, the deformation textures remain virtually unaffected except for a general texture sharpening by up to 20 pct. Under certain circumstances—*e.g.*, in the presence of precipitation occurring concurrently with recrystallization—recovery is so extended that essentially the entire excess dislocation density is removed through recovery.[95] In most cases, by contrast, recovery reactions give rise to the formation

of recrystallization nuclei which, after a certain incubation period, appear at distinct locations in the as-deformed microstructure. During further annealing these nuclei grow until they impinge with other growing grains. In commercial aluminum alloys, these processes are inevitably complicated by the presence of both small and large particles.[95]

The microstructural changes during recrystallization are thus based on the two fundamental mechanisms of nucleation and growth. In Al alloys, the orientations of every recrystallization nucleus must already exist in the as-deformed microstructure (so-called preformed nuclei[96]). However, any potential nuclei must possess a mobile grain boundary with respect to the surrounding matrix. This requires mobile, *i.e.*, high-angle grain boundaries with misorientations exceeding 15 deg, whereas recovery in the deformed matrix only provides misorientations that scarcely exceed 10 deg. Consequently, nucleation is generally restricted to sites in the vicinity of major deformation inhomogeneities. In heavily rolled Al alloys, four different nucleation sites are of most importance, namely cube bands, the preexisting grain boundaries, shear bands and the deformation zones around large particles. The recrystallization textures of industrially processed Al alloys then emerge from a competition during the growth of the grains stemming from these four nucleation sites.[97]

Today, nucleation and growth of recrystallization can be readily studied by EBSD. In particular the combination of a spatial resolution in the sub-micron range and continuously increasing scanning speed enables analysis of large areas which cover sufficient nucleation events to provide results with statistical significance.[98] As an example, Schäfer and Gottstein applied high-resolution EBSD measurements to elucidate the nucleation and growth mechanisms of particle stimulated nucleation (PSN) in a particle-containing Al alloy.[99] Similarly, Sukhopar and Gottstein analyzed the spatial distribution of cube-oriented nuclei in a cold-rolled Al alloy and used this information as an input for a subsequent simulation with a cellular automaton approach.[100]

However, EBSD usually provides maps only in 2D, while construction of 3D information requires techniques of serial sectioning. Over the past 15 years a novel technique, referred to as three-dimensional X-ray diffraction (3DXRD), has been advanced for generating a truly 3D map of the microstructure.[101,102] The 3DXRD techniques have been developed in cooperation between Risø National Laboratory, Denmark, and the European Synchrotron Radiation Facility (ESRF) in Grenoble, France.[103] Based on the use of highly penetrating hard X-rays and a "tomographic" approach to diffraction, the method enables a non-destructive 3D description of the microtexture and microstructure within polycrystals. With this technique, the growth of new grains during recrystallization can be traced *in situ*, and "movies" revealing the 3D growth of bulk recrystallizing grains can be recorded.[104] Such analysis has revealed that the growth of recrystallizing grains is highly heterogeneous, the shape of the grains very irregular, and the migration of the grain boundaries often does not occur smoothly but step by step. Thus, 3DXRD provides information about the four-dimensional evolution of recrystallizing grains as a function of location and time.

Nucleation of recrystallization has also been studied by 3DXRD. Here, research has focused on *in situ* measurements of the orientation relationships between the nuclei and the regions around the specific nucleation sites before annealing. So far, only a few such studies have been conducted, and it has been observed that nuclei with new orientations, *i.e.*, orientations *not* observed in the parent deformed matrix, may evolve,[105] which is in contradiction to the common assumption of "preformed nuclei". (*e.g.*, References 96 and 97) However, for characterization of fine-scale deformation structures where nucleation usually takes place the spatial resolution of 3DXRD turned out to be insufficient. Higher spatial resolution was achieved with a technique called differential aperture X-ray microscopy (DAXM) with polychromatic synchrotron radiation[106] to advance the direct observation of nucleation. This technique indicated that nuclei develop at sites of high stored energy and they indeed inherit orientations that are already present in the deformed matrix.[107]

More recently, EBSD has been coupled with a focused ion beam (FIB) to form a useful tool for producing high-resolution crystallographic information in reasonably large microstructure volumes.[108] The FIB is used as a high-precision serial sectioning device for generating consecutive milled surfaces which are then mapped by EBSD. Finally, the EBSD maps are combined to generate 3D microstructure information. This technique allows the full crystallographic characterization of all kinds of interfaces, comprising the morphology and the crystallographic indices of the interface planes. Thus, this technique is able to reveal recrystallization features that are not clearly evident in 2D EBSD maps such as clear evidence of particle stimulated nucleation of recrystallization.[109]

VI. MODELING AND SIMULATION

A. *Introduction to Modeling Methodologies*

Microstructural models can be categorized into mean field and microstructural simulation approaches. Mean-field models track microstructure in terms of volume averaged parameters such as precipitate number density, volume fraction of transformation, or average grain size. Microstructural simulations aim to provide a faithful reproduction of the microstructure to be directly correlated with experimental observation; this includes capturing the distribution of all microstructural features in space as well as their evolution with time.

Good thermodynamic models are essential in microstructural modeling to define the equilibrium state and describe the energy changes driving microstructural change. The Calphad method[110] remains the most commonly used to describe the equilibrium thermodynamics of multicomponent aluminum alloys. This method relies on accurately assessed experimental data for the systems of concern, captured in thermodynamic

databases. Atomistic simulation methods such as those based on density functional theory (DFT) can help by enabling *ab-initio* calculation of thermodynamic parameters.[111,112]

A key challenge in modeling microstructure in wrought aluminum alloys is the importance of heterogeneity in controlling behavior. Capturing this heterogeneity in a statistical way is required so that it can be condensed into an effective volume that is tractable by full field microstructural simulation. In recent years the representative volume element (RVE) concept[113] has gained popularity for this purpose. Pioneering research has also been performed in aluminum alloys to integrate microstructural models into process models for the purpose simulating the entire fabrication chain for aluminum components.[114]

B. *Modeling of Precipitation*

Second-phase precipitation is critical to the properties of many aluminum alloys and thus precipitation has been the focus of many modeling efforts. Mean-field precipitation models based on classical kinetic theory are now widely applied and available in commercial packages (*e.g.*, MatCalc, TC-Prisma, PrecipiCalc, ClaNG). Many of these models are based on the numerical framework developed by Kampann and Wagner (KWN[115]) in which the precipitate size distribution is discretized into size classes whose evolution is tracked by numerical integration, subject to classical nucleation and growth theory. At each time-step, the mean-field assumption is used to calculate the remaining matrix composition, and in this way the processes of nucleation, growth, and coarsening evolve ''naturally'' and are able to overlap in a physically reasonable way. The basic KWN method has been extended for aluminum alloys in a number of important ways including allowing competitive heterogeneous nucleation at different sites,[54] non-spherical precipitates,[116,117] non-uniform initial composition,[118] and precipitate sequences.[119–121] Figure 5 shows an example of the prediction of the evolution of phases, both constituents and dispersoids, during homogenization of alloy AA5083, performed using the ClaNG model.[122] In addition to this model, the KWN method also provides the precipitation prediction in integrated simulations such as the NaMo model for 6xxx alloys[123] and integrated process-microstructure-property modeling for friction stir welding of aluminum alloys.[124]

A limitation of the KWN model is its use of classical nucleation theory. The nucleation process is one of the most difficult to model since it involves small numbers of atoms and is not directly observable. Modern atomistic modeling methods such as kinetic Monte Carlo coupled with a cluster expansion of the energy or, alternatively, a cluster dynamics approach provides more realistic methods for simulating nucleation, and can be useful in describing the early stages of precipitation ageing.[56,125–129]

Microstructural simulation for precipitation has gained increasing prominence in the last decade. The most widely used approach is the phase field method (PFM).[130] The PFM is now sufficiently powerful to treat the growth/coarsening of precipitates and their heterogeneities within a microstructure.[131–135] Given the correct thermodynamic and kinetic (diffusion) parameters, the PFM gives an evolving full field prediction of the microstructure in which the competition between precipitation sites, precipitate free zones, and anisotropic precipitate morphologies arise naturally. An example output from such a calculation for θ' precipitation in Al-Cu is shown in Figure 6(a).[134] The PFM can also be extended to include plasticity, for example to study the interaction between precipitates and dislocations (*e.g.*, Figure 6(b)[135]).

C. *Modeling of Deformation and Recrystallization*

Modeling deformation requires a consideration of all length scales, from individual dislocation behavior at the atomic scale through the mesoscale to macroscale deformation at the component level. Scale bridging, itself a considerable challenge, is then needed to link these different regimes. Atomistic and dislocation dynamics simulations in aluminum are now significantly advanced (*e.g.*, References 136 and 137), and show good capability in faithfully reproducing complex effects such as dislocation interactions with shearable precipitates down to the atomic scale.[136]

The effect of deformation on microstructure and texture at the mesoscale can be predicted using crystal-plasticity models, which can be divided into mean-field and spatially resolved approaches in an analogous way to precipitation modeling. In crystal-plasticity modeling, the individual crystallites are assumed to deform by slip on a number of crystallographic slip systems, so as to accommodate the macroscopic strain state. The classical mean-field Taylor-type models or self-consistent models[138] are indeed capable of simulating the main features of typical rolling textures, yet they are inadequate to reproduce details in the texture evolution. The main reason for this poor texture simulation may be ascribed to the fact that they do not take grain-to-grain interaction into consideration, treating all grains of the same orientation identically. More advanced multi-grain or *N*-point formulations—like the LAMEL model[139,140] or the grain interaction (GIA) model[141]—indeed yield a significantly reduced rate of texture evolution and, in consequence, more realistic rolling textures.[142,143]

An alternative approach to tackle grain interaction is the use of crystal-plasticity-based finite element models (CP-FEM) which incorporate crystal-plasticity constitutive equations into finite element codes.[144,145] The RVE concept is used to reduce the number of grains in the simulation to be manageable in the computation, and care must be taken to optimize the number of elements in the RVE (*e.g.*, Figure 7[144]). CP-FEM has proved very valuable in tackling queries involving low deformations, including tensile and compression tests, or anisotropy and sheet formability. For heavy bulk deformation as encountered in rolling or extrusion the CP-FEM predictions are usually not as good as may be

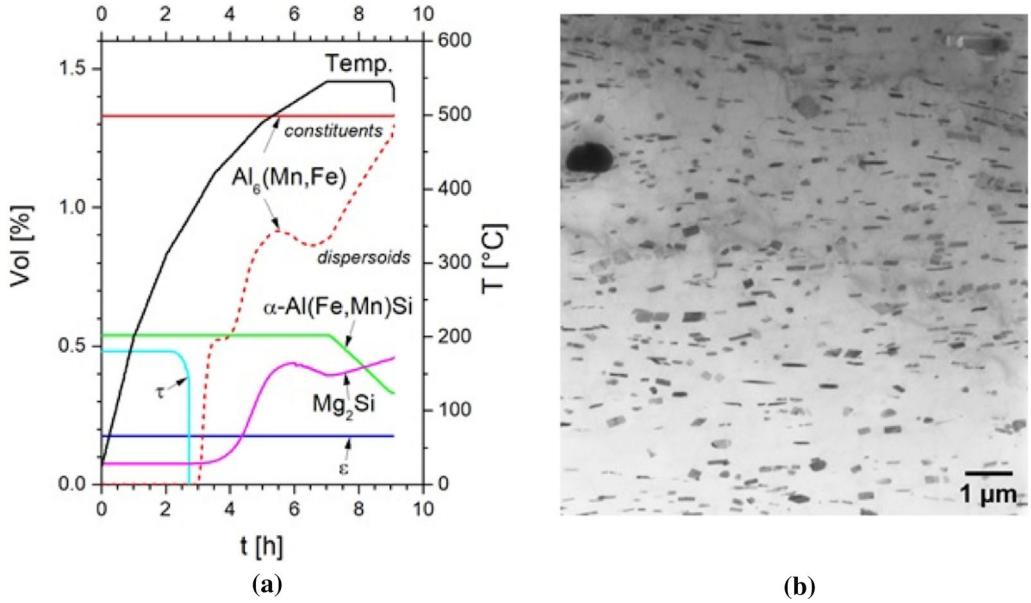

Fig. 5—(*a*) ClaNG simulation of the evolution of second-phase particles during homogenization of alloy AA5083. (*b*) TEM micrograph showing the dispersoids in the homogenized state.[122]

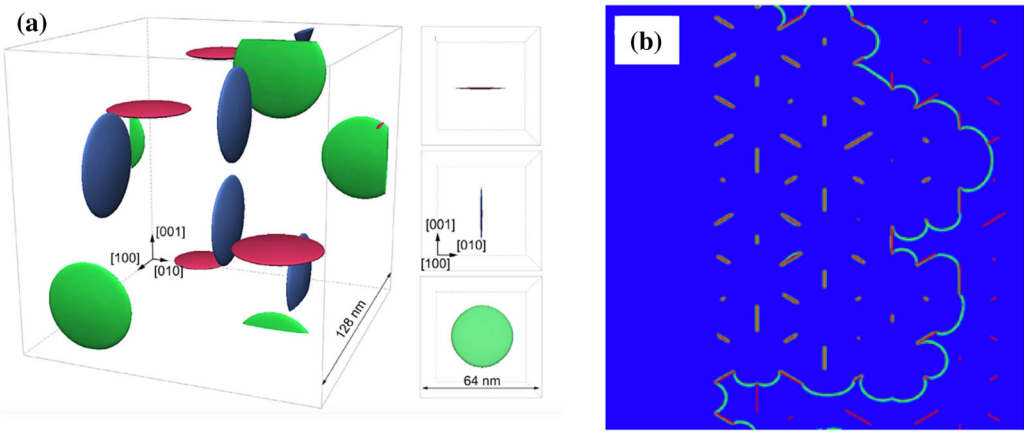

Fig. 6—(*a*) Phase field prediction of θ' precipitation in Al-Cu alloy.[134] (*b*) Phase field prediction of dislocation motion through a distribution of coherent θ' precipitate plates.[135] Figure reproduced from Ref. [134] with permission from Elsevier.

expected, but still perform better than the standard 1-point polycrystal-plasticity approaches.

Crystal-plasticity models may be coupled to recrystallization models, this provides a full through process simulation of texture and grain structure (*e.g.*, Reference 146). Such models can be integrated into a wider framework that includes full field precipitation modeling, recrystallization, and damage prediction (during deformation) (*e.g.*, Reference 147). Alternative approaches to full field modeling of recrystallization and grain growth include the cellular automata or vertex tracking methods, with further details given elsewhere.[148–150] Scale bridging through the RVE approach enables microstructural information to be explicitly captured in process and performance models at the component level.[147]

VII. SUMMARY

Understanding and control of microstructure is central to understanding and control of properties in wrought aluminum alloys and is thus of both great practical and scientific importance. Over the past decade, developments in characterization tools that allow analysis from the atomic to the microstructural scale, in 3-dimensions, in real time (*in situ*) have greatly added to our knowledge of microstructural control in wrought aluminum alloys.

In tandem with the developments in characterization, the capabilities in modeling and simulation have been greatly enhanced both by improvements in computing hardware and new modeling tools. Full field microstructural simulation is now practically possible for realistic volumes of microstructure, and scale bridging

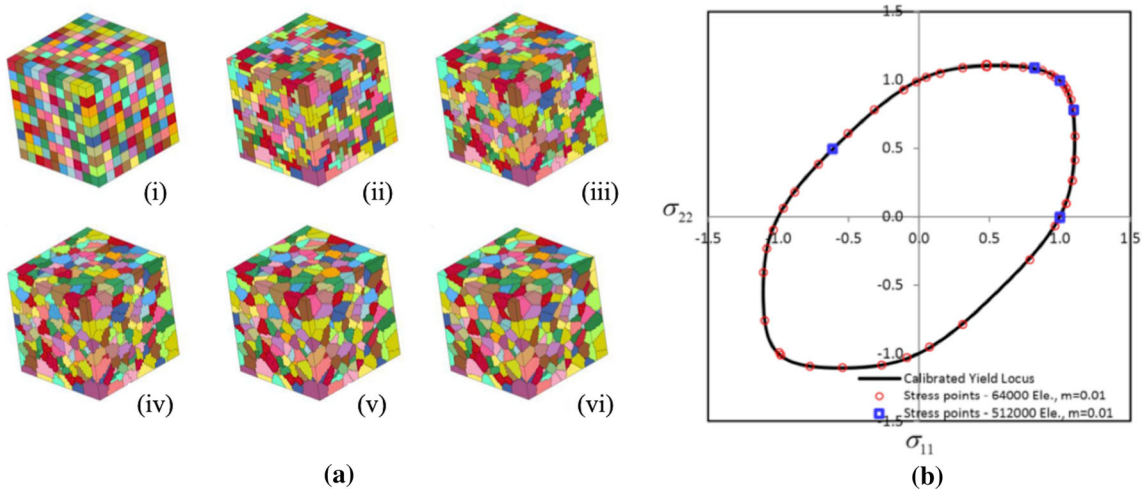

Fig. 7—(*a*) Finite element meshes of an RVE with 1000 to 512,000 elements (i to vi). (*b*) Predicted yield locus computed by CP-FEM with RVEs of 64000 and 512,000 elements.[144] Figure reproduced from Ref. [144] with permission from Elsevier.

techniques are now established to link from the atomistic to component scale. There remain some phenomena where microstructural understanding is not yet sufficiently advanced to allow physics-based simulation, an example being the clustering in 6xxx automotive alloys and the resulting effect on formability. Nevertheless, in many cases, design of alloys and microstructures *in silico* is now a practical reality, offering exciting new opportunities to develop high performance, sustainable aluminum alloy solutions.

OPEN ACCESS

REFERENCES

1. http://www.world-aluminium.org/statistics/, http://www.world-aluminium.org/statistics/ (World Aluminum, 2019).
2. J.D. Embury, D.J. Lloyd, and T.R. Ramachandran: *Aluminum Alloys-Contemporary Research and Applications*, Academic Press Inc, New York, 1989, pp. 579–601.
3. A. Guinier: *Nature*, 1938, vol. 142, p. 569.
4. G.D. Preston: *Nature*, 1938, vol. 142, p. 570.
5. R.B. Nicholson and J. Nutting: *Philos. Mag. A*, 1958, vol. 3, pp. 531–35.
6. M. Karlik and B. Jouffrey: *Acta Mater.*, 1997, vol. 45, pp. 3251–63.
7. F. De Geuser and A. Deschamps: *C R Phys.*, 2012, vol. 13, pp. 246–56.
8. M.K. Miller, T.F. Kelly, K. Rajan, and S.P. Ringer: *Mater. Today*, 2012, vol. 15, pp. 158–65.
9. S.P. Ringer, K. Hono, I.J. Polmear, and T. Sakurai: *Acta Mater.*, 1996, vol. 44, pp. 1883–98.
10. Y. Nagai, M. Murayama, Z. Tang, T. Nonaka, K. Hono, and M. Hasegawa: *Acta Mater.*, 2001, vol. 49, pp. 913–20.
11. L. Couturier, A. Deschamps, F. De Geuser, F. Fazeli, and W.J. Poole: *Scripta Mater.*, 2017, vol. 136, pp. 120–23.
12. F. De Geuser, M.J. Styles, C.R. Hutchinson, and A. Deschamps: *Acta Mater.*, 2015, vol. 101, pp. 1–9.
13. V. Araullo-Peters, B. Gault, F. De Geuser, A. Deschamps, and J.M. Cairney: *Acta Mater.*, 2014, vol. 66, pp. 199–208.
14. E. Gumbmann, W. Lefebvre, F. De Geuser, C. Sigli, and A. Deschamps: *Acta Mater.*, 2016, vol. 115, pp. 104–14.
15. E. Gumbmann, F. De Geuser, C. Sigli, and A. Deschamps: *Acta Mater.*, 2017, vol. 133, pp. 172–85.
16. Y. Zheng, Y. Liu, N. Wilson, S. Liu, X. Zhao, H. Chen, J. Li, Z. Zheng, L. Bourgeois, and J.-F. Nie: *Acta Mater.*, 2020, vol. 184, pp. 17–29.
17. C. Sigli, F. De Geuser, A. Deschamps, J. Lépinoux, and M. Perez: *C R Phys.*, 2018, vol. 19, pp. 688–709.
18. S.P. Ringer, T. Sakurai, and I.J. Polmear: *Acta Mater.*, 1997, vol. 45, pp. 3731–44.
19. W.M. Rainforth, L.M. Rylands, and H. Jones: *Scripta Mater.*, 1996, vol. 35, pp. 261–65.
20. W.A. Cassada, G.J. Shiflet, and E.A. Starke: *Metall. Trans. A*, 1991, vol. 22, pp. 287–97.
21. B. Decreus, A. Deschamps, F. De Geuser, P. Donnadieu, C. Sigli, and M. Weyland: *Acta Mater.*, 2013, vol. 61, pp. 2207–18.
22. P. Donnadieu, Y. Shao, F. De Geuser, G.A. Botton, S. Lazar, M. Cheynet, M. de Boissieu, and A. Deschamps: *Acta Mater.*, 2011, vol. 59, pp. 462–72.
23. C. Dwyer, M. Weyland, L.Y. Chang, and B.C. Muddle: *Appl. Phys. Lett.*, 2011, vol. 98, p. 201909.
24. A. Deschamps, B. Decreus, F. De Geuser, T. Dorin, and M. Weyland: *Acta Mater.*, 2013, vol. 61, pp. 4010–21.
25. T. Maeda, K. Kaneko, T. Namba, Y. Koshino, Y. Sato, R. Teranishi, and Y. Aruga: *Sci Rep*, 2018, vol. 8, p. 16629.
26. G.A. Edwards, K. Stiller, G.L. Dunlop, and M.J. Couper: *Acta Mater.*, 1998, vol. 46, pp. 3893–3904.
27. S.J. Andersen, H.W. Zandbergen, J. Jansen, C. Traeholt, U. Tundal, and O. Reiso: *Acta Mater.*, 1998, vol. 46, pp. 3283–98.

28. R. Vissers, M.A. van Huis, J. Jansen, H.W. Zandbergen, C.D. Marioara, and S.J. Andersen: *Acta Mater.*, 2007, vol. 55, pp. 3815–23.
29. P.H. Ninive, A. Strandlie, S. Gulbrandsen-Dahl, W. Lefebvre, C.D. Marioara, S.J. Andersen, J. Friis, R. Holmestad, and O.M. Løvvik: *Acta Mater.*, 2014, vol. 69, pp. 126–34.
30. H.S. Hasting, A.G. Froseth, S.J. Andersen, R. Vissers, J.C. Walmsley, C.D. Marioara, F. Danoix, W. Lefebvre, and R. Holmestad: *J. Applied Physics*, 2009, vol. 106, pp. 123527-1–527-9.
31. E. Christiansen, C.D. Marioara, B. Holmedal, O.S. Hopperstad, and R. Holmestad: *Sci. Rep.*, 2019, vol. 9, p. 17446.
32. C. Marioara, S.J. Andersen, J. Royset, O. Reiso S. Gulbrandsen-Dahl, T.E. Nicolaisen, I.R. Opheim, J.F. Helgaker, and R. Holmestad: *Metall. Mater. Trans. A*, 2014, vol. 45A, pp. 2938–49.
33. C. Flament, J. Ribis, J. Garnier, Y. Serruys, F. Lepretre, A. Gentils, C. Baumier, M. Descoins, D. Mangelinck, A. Lopez, K. Colas, K. Buchanan, P. Donnadieu, and A. Deschamps: *Acta Mater.*, 2017, vol. 128, pp. 64–76.
34. A. Mossad Ali, A.-F. Gaber, K. Matsuda, and S. Ikeno: *Mater. Chem. Phys.*, 2014, vol. 147, pp. 461–68.
35. T. Saito, C.D. Marioara, S.J. Andersen, W. Lefebvre, and R. Holmestad: *Phil. Mag.*, 2014, vol. 94, pp. 520–31.
36. K. Li, A. Beche, M. Song, G. Sha, X. Lu, K. Zhang, Y. Du, S.P. Ringer, and D. Schryvers: *Scripta Mater.*, 2014, vol. 75, pp. 86–89.
37. X. Sauvage, S. Lee, K. Matsuda, and Z. Horita: *J. Alloys Compd.*, 2017, vol. 710, pp. 199–204.
38. L. Ding, Z. Jia, J.-F. Nie, Y. Weng, L. Cao, H. Chen, X. Wu, and Q. Liu: *Acta Mater.*, 2018, vol. 145, pp. 437–50.
39. A. Bobel, K. Kim, C. Wolverton, M. Walker, and G.B. Olson: *Acta Mater.*, 2017, vol. 138, pp. 150–60.
40. Y. Weng, L. Ding, Z. Zhang, Z. Jia, B. Wen, Y. Liu, S. Muraishi, Y. Li, and Q. Liu: *Acta Mater.*, 2019, vol. 180, pp. 301–16.
41. P. Schuster, J. Österreicher, G. Kirov, C. Sommitsch, O. Kessler, and E. Mukeli: *Metals*, 2019, vol. 9, p. 305.
42. N.J.H. Holroyd and G.M. Scamans: *Metall. Mater. Trans. A*, 2011, vol. 42A, pp. 3979–98.
43. M. Talianker and B. Cina: *Metall. Trans. A*, 1989, vol. 20A, pp. 2087–92.
44. S.P. Knight, K. Pohl, N.J.H. Holroyd, N. Birbilis, P.A. Rometsch, B.C. Muddle, R. Goswami, and S.P. Lynch: *Corros. Sci.*, 2015, vol. 98, pp. 50–62.
45. H. Zhao, F. De Geuser, A. Kwiatkowski da Silva, A. Szczepaniak, B. Gault, D. Ponge, and D. Raabe: *Acta Mater.*, 2018, vol. 156, pp. 318–29.
46. Y.-Y. Li, L. Kovarik, P.J. Phillips, Y.-F. Hsu, W.-H. Wang, and M.J. Mills: *Philos. Mag. Lett.*, 2012, vol. 92, pp. 166–78.
47. T. Marlaud, A. Deschamps, F. Bley, W. Lefebvre, and B. Baroux: *Acta Mater.*, 2010, vol. 58, pp. 248–60.
48. S.P. Knight, N. Birbilis, B.C. Muddle, A.R. Trueman, and S.P. Lynch: *Corros. Sci.*, 2010, vol. 52, pp. 4073–80.
49. R. A. Michi, J. P. Toinin, D. N. Seidman and D. C Dunand, *Mater. Sci. Eng. A*, 2019, pp. 78–89.
50. K.E. Knipling, D.C. Dunand, and D.N. Seidman: *Z. Metall.*, 2006, vol. 97, pp. 246–65.
51. E.A. Marquis and D.N. Seidman: *Acta Mater.*, 2001, vol. 49, pp. 1909–19.
52. V.M. Glazov, G.P. Lazarev, and G.A. Korol'kov: *Met. Sci. Heat Treat.*, 1959, vol. 1, pp. 51–53.
53. A. De Luca, D.N. Seidman, and D.C. Dunand: *Acta Mater.*, 2019, vol. 165, pp. 1–14.
54. J.D. Robson: *Acta Mater.*, 2004, vol. 52, pp. 1409–21.
55. B. Forbord, W. Lefebvre, F. Danoix, H. Hallem, and K. Marthinsen: *Scripta Mater.*, 2004, vol. 51, pp. 333–37.
56. E. Clouet, L. Laé, T. Epicier, W. Lefebvre, M. Nastar, and A. Deschamps: *Nat. Mater.*, 2006, vol. 5, pp. 482–88.
57. C. Booth-Morrison, Z. Mao, M. Diaz, D.C. Dunand, C. Wolverton, and D.N. Seidman: *Acta Mater.*, 2012, vol. 60, pp. 4740–52.
58. L. Litynska, D. Abou-Ras, G. Kostorz, and J. Dutkiewicz: *J. Microsc.*, 2006, vol. 223, pp. 182–84.
59. G. Sha and A. Cerezo: *Ultramicroscopy*, 2005, vol. 102, pp. 151–59.
60. A.M. Cassell, J.D. Robson, C.P. Race, A. Eggeman, T. Hashimoto, and M. Besel: *Acta Mater.*, 2019, vol. 169, pp. 135–46.
61. T. J. Langan and T. Dorin, US2019/0249283A1, 2019, pp 1–7.
62. H. Zhong, P.A. Rometsch, X. Wu, L. Cao, and Y. Estrin: *Mater. Sci. Eng. A*, 2017, vol. A697, pp. 79–85.
63. O. Engler, C.D. Marioara, Y. Aruga, M. Kozuka, and O.R. Myhr: *Mater. Sci. Eng. A*, 2019, vol. 759, pp. 520–29.
64. F. De Geuser and B. Gault: *Acta Mater.*, 2020, vol. 188, pp. 406–15.
65. Z. Peng, F. Vurpillot, P.-P. Choi, Y. Li, D. Raabe, and B. Gault: *Ultramicroscopy*, 2018, vol. 189, pp. 54–60.
66. R. K. W. Marceau, A. de Vaucorbeil, G. Sha, S. P. Ringer and W. J. Poole, *Acta Materialia* 2013.
67. M.J. Starink, L.F. Cao, and P.A. Rometsch: *Acta Mater.*, 2012, vol. 60, pp. 4194–207.
68. A. de Vaucorbeil, C.W. Sinclair, and W.J. Poole: *Materialia*, 2018, vol. 4, pp. 566–74.
69. S. Pogatscher, H. Antrekowitsch, H. Leitner, T. Ebner, and P.J. Uggowitzer: *Acta Mater.*, 2011, vol. 59, pp. 3352–63.
70. D. Dumitraschkewitz, P.J. Uggowitzer, S.A. Gerst, J.F. Löffler, and S. Pogatscher: *Nat. Commun.*, 2019, vol. 10, p. 4746.
71. W. Sun, Y. Zhu, R. Marceau, Li. Wang, Q. Zhang, X. Gao and C. R. Hutchinson, *Science* 2019, vol. 363, pp. 972–75.
72. J.D. Embury, A. Deschamps, and Y. Brechet: *Scripta Mater.*, 2003, vol. 49, pp. 927–32.
73. C.R. Hutchinson, F. de Geuser, Y. Chen, and A. Deschamps: *Acta Mater.*, 2014, vol. 74, pp. 96–109.
74. A. Deschamps, G. Fribourg, Y. Bréchet, J.L. Chemin, and C.R. Hutchinson: *Acta Mater.*, 2012, vol. 60, pp. 1905–16.
75. A. Deschamps, F. Livet, and Y. Bréchet: *Acta Mater.*, 1998, vol. 47, pp. 281–92.
76. A. Deschamps and Y. Bréchet: *Acta Mater.*, 1998, vol. 47, pp. 293–305.
77. C.R. Hutchinson, P.T. Loo, T.J. Bastow, A.J. Hill, and J. da Costa Teixeira: *Acta Mater.*, 2009, vol. 57, pp. 5645–53.
78. Z.M. Wang and G.J. Shiflet: *Metall. Mater. Trans. A*, 1998, vol. 29A, pp. 2073–85.
79. J.D. Robson, T. Hill, and N. Kamp: *Mater. Sci. Forum*, 2014, vols. 794–796, pp. 697–703.
80. B. Milkereit, M.J. Starink, P.A. Rometsch, C. Schick, and O. Kessler: *Materials (Basel)*, 2019, vol. 12, p. 4083.
81. R. Nadella, D.G. Eskin, Q. Du, and L. Katgerman: *Prog. Mater. Sci.*, 2008, vol. 53, pp. 421–80.
82. J. Sarkar, T.R.G. Kutty, K.T. Conlon, D.S. Wilkinson, J.D. Embury, and D.J. Lloyd: *Mater. Sci. Eng. A*, 2001, vol. A316, pp. 52–59.
83. J. Sarkar, T.R.G. Kutty, D.S. Wilkinson, J.D. Embury, and D.J. Lloyd: *Mater. Sci. Eng. A*, 2004, vol. A369, pp. 258–66.
84. L. Sweet, S.M. Zhu, S.X. Gao, J.A. Taylor, and M.A. Easton: *Metall. Mater. Trans. A*, 2011, vol. 42A, pp. 1737–49.
85. D.T.L. Alexander and A.L. Greer: *Acta Mater.*, 2002, vol. 50, pp. 2571–83.
86. N.C.W. Kuijpers, F.J. Vermolen, C. Vuik, P.T.G. Koenis, K.E. Nilsen, and S. Van der Zwagg: *Mater. Sci. Eng. A*, 2005, vol. A394, pp. 9–19.
87. P. Priya, D.R. Johnson, and J.M. Krane: *Metall. Mater. Trans. A*, 2016, vol. 47A, pp. 4625–39.
88. Q. Du, W.J. Poole, and M.A. Wells: *Acta Mater.*, 2012, vol. 60, pp. 3830–39.
89. Q. Du, W.J. Poole, M.A. Wells, and N.C. Parson: *Acta Mater.*, 2013, vol. 61, pp. 4961–73.
90. C.L. Liu, Q. Du, N.C. Parson, and W.J. Poole: *Scripta Mater.*, 2018, vol. 152, pp. 59–63.
91. J.D. Robson: *Encyclopedia of Aluminum and Its Alloys*, CRC Press, Boca Raton, 2019, pp. 770–78.
92. L. Lodgaard and N. Ryum: *Mater. Sci. Eng. A*, 2000, vol. 283, pp. 144–52.
93. F.J. Humphreys and M. Hatherley: *Recrystallization and Related Annealing Phenomena*, Elsevier, Amsterdam, 2004.
94. O. Engler and J. Aegerter: *Materf. Sci. Eng. A*, 2014, vol. 618, pp. 663–71.
95. K. Huang, K. Marthinsen, Q. Zhao, and R.E. Logé: *Prog. Mater. Sci.*, 2018, vol. 92, pp. 284–359.

96. R.D. Doherty, D.A. Hughes, F.J. Humphreys, J.J. Jonas, D. Juul-Jensen, M.E. Kassner, W.E. King, T.R. McNelley, H.J. McQueen, and A.D. Rollett: *Mater. Sci. Eng. A*, 1997, vol. A238, pp. 219–74.
97. O. Engler: *Mater. Sci. Technol.*, 1996, vol. 12, pp. 859–72.
98. O. Engler and V. Randle: *Introduction to Texture Analysis: Macrotexture, Microtexture and Orientation Mapping*, 2nd ed., CRC Press, Bota Raton, FL, 2010.
99. C. Schäfer and G. Gottstein: *Int. J. Mater. Res.*, 2011, vol. 102, pp. 1106–14.
100. O. Sukhopar and G. Gottstein: *Int. J. Mater. Res.*, 2016, vol. 107, pp. 979–87.
101. H.F. Poulsen, S.F. Nielsen, E.M. Lauridsen, S. Schmidt, R.M. Suter, U. Lienert, L. Margulies, T. Lorentzen, and D. Juul-Jensen: *J. Appl. Crystallogr*, 2001, vol. 34, pp. 751–56.
102. D. Juul Jensen, E.M. Lauridsen, H.F. Poulsen, S. Schmidt, H.O. Sorensen, and G.B.M. Vaughan: *Mater. Today*, 2006, vol. 9, pp. 18–25.
103. C. Zhang, Y. Zhang, G. Wu, W. Liu, R. Xu, D. Juul Jensen, and A. Godfrey: *J. Appl. Crystallogr.*, 2019, vol. 52, pp. 1119–27.
104. D. Juul Jensen and H.F. Poulsen: *Mater. Charateriz.*, 2012, vol. 72, pp. 1–7.
105. S.S. West, S. Schmidt, H.O. Sørensen, G. Winther, H.F. Poulsen, L. Margulies, C. Gundlach, and D. Juul Jensen: *Scripta mater.*, 2009, vol. 61, pp. 875–78.
106. B.C. Larson, W. Yang, G.E. Ice, J.D. Budai, and J.Z. Tischler: *Nature*, 2002, vol. 415, pp. 887–90.
107. C. Xu, Y. Zhang, A. Godfrey, G. Wu, W. Liu, J.Z. Tischler, Q. Liu, and D. Juul Jensen: *Sci. Rep.*, 2017, vol. 7, p. 42508.
108. S. Zaefferer, S.I. Wright, and D. Raabe: *Metall. Mater. Trans. A*, 2008, vol. 39A, pp. 374–89.
109. F.J. Humphreys, P.S. Bate, A. Gholinia, and I. Brough: *Mater. Sci. Forum*, 2012, vols. 715–716, pp. 23–32.
110. B. Sundman, U.R. Kattner, C. Sigli, M. Stratmann, R. Le Tellier, M. Palumbo, and S.G. Fries: *Comput. Mater. Sci.*, 2016, vol. 125, pp. 188–96.
111. X. Zhang and S. Wang: *Comput. Mater. Sci.*, 2014, vol. 90, pp. 56–60.
112. H. Zhang, Y. Wang, S.L. Shang, C. Ravi, C. Wolverton, L.Q. Chen, and Z.K. Liu: *Calphad*, 2010, vol. 34, pp. 20–25.
113. M. Diehl, M. Groeber, C. Haase, D.A. Molodov, F. Roters, and D. Raabe: *JOM*, 2017, vol. 69, pp. 848–55.
114. J. Hirsch: *Virtual Fabrication of Aluminum Products*, Wiley-VCH, New York, 2007.
115. R. Wagner and R. Kampmann: *Phase Transform. Mater.*, 1991, vol. 5, pp. 213–303.
116. D. Bardel, M. Perez, D. Nelias, A. Deschamps, C.R. Hutchinson, D. Maisonnette, T. Chaise, J. Garnier, and F. Bourlier: *Acta Mater.*, 2014, vol. 62, pp. 129–40.
117. B. Holmedal, E. Osmundsen, and Q. Du: *Metall. Mater. Trans. A*, 2015, vol. 47A, pp. 581–88.
118. J.D. Robson and P.B. Prangnell: *Acta Mater.*, 2001, vol. 49, pp. 599–613.
119. N. Kamp, A. Sullivan, R. Tomasi, and J.D. Robson: *Acta Mater.*, 2006, vol. 54, pp. 2003–14.
120. B. Holmedal, E. Osmundsen, and Q. Du: *Metall. Mater. Trans. A*, 2016, vol. 47A, pp. 581–88.
121. Q. Du, K. Tang, C.D. Marioara, S.J. Andersen, B. Holmedal, and R. Holmestad: *Acta Mater.*, 2017, vol. 122, pp. 178–86.
122. O. Engler and S. Miller-Jupp: *J. Alloys Compd.*, 2016, vol. 689, pp. 998–1010.
123. O.R. Myhr, O.S. Hopperstad, and T. Børvik: *Metall. Mater. Trans. A*, 2018, vol. 49A, pp. 3592–3609.
124. A. Simar, Y. Bréchet, B. de Meester, A. Denquin, C. Gallais, and T. Pardoen: *Prog. Mater Sci.*, 2012, vol. 57, pp. 95–183.
125. E. Clouet, M. Nastar, and C. Sigli: *Phys. Rev. B*, 2004, vol. 69, p. 064109.
126. X. Zhang: PhD Thesis, Delft University of Technology, 2017.
127. X. Zhang and M.H.F. Sluiter: *J. Phase Equilib. Diffus.*, 2016, vol. 37, pp. 44–52.
128. O.I. Gorbatov, A.Y. Stroev, Y.N. Gornostyrev, and P.A. Korzhavyi: *Acta Mater.*, 2019, vol. 179, pp. 70–84.
129. T. Stegmüller and F. Haider: *Acta Mater.*, 2019, vol. 177, pp. 240–49.
130. L.-Q. Chen and Y. Wang: *JOM*, 1996, vol. 48, pp. 13–18.
131. V. Vaithyanathan, C. Wolverton, and L.Q. Chen: *Acta Mater.*, 2004, vol. 52, pp. 2973–87.
132. I. Häusler, C. Schwarze, M.U. Bilal, D.V. Ramirez, W. Hetaba, R.D. Kamachali, and B. Skrotzki: *Materials*, 2017, vol. 10, p. 117.
133. K. Kim, A. Roy, M.P. Gururajan, C. Wolverton, and P.W. Voorhees: *Acta Mater.*, 2017, vol. 140, pp. 344–54.
134. H. Liu, I. Papadimitriou, F.X. Lin, and J.L. Lorca: *Acta Mater.*, 2019, vol. 167, pp. 121–35.
135. H. Liu, Y. Gao, L. Qi, Y. Wang, and J.-F. Nie: *Metall. Mater. Trans. A*, 2015, vol. 46A, pp. 3287–301.
136. R. Santos-Güemes, B. Bellón, G. Esteban-Manzanares, J. Segurado, L. Capolungo, and J.L. Lorca: *Acta Mater.*, 2020, vol. 188, pp. 475–85.
137. G. Esteban-Manzanares, B. Bellón, E. Martínez, I. Papadimitriou, and J.L. Lorca: *J. Mech. Phys. Solids*, 2019, vol. 132, p. 103675.
138. R.A. Lebensohn and C.N. Tomé: *Acta Metall. Mater.*, 1993, vol. 41, pp. 2611–24.
139. P. Van Houtte, S. Li, M. Seefeldt, and L. Delannay: *Int. J. Plastic*, 2005, vol. 21, pp. 589–624.
140. T. Mánik and B. Holmedal: *Mater. Sci. Eng. A*, 2013, vol. 580, pp. 349–54.
141. M. Crumbach, G. Pomana, P. Wagner and G. A. Gottstein: in *Proceedings of the First Joint International Conference on Recrystallisation and Grain Growth*, ed. G. Gottstein and D. A. Molodov, Springer, Berlin, 2001, pp 1053–60.
142. P. Van Houtte, S. Li, and O. Engler: *Aluminium*, 2004, vol. 80, pp. 702–06.
143. O. Engler, M. Crumbach, and S. Li: *Acta Mater.*, 2005, vol. 53, pp. 2241–57.
144. K. Zhang, B. Holmedal, T. Mánika, and A. Saai: *Int. J. Plastic.*, 2019, vol. 114, pp. 144–60.
145. F. Roters, P. Eisenlohr, L. Hantcherli, D.D. Tjahjanto, T.R. Bieler, and D. Raabe: *Acta Mater.*, 2010, vol. 58, pp. 1152–1211.
146. M. Crumbach, M. Goerdeler, G. Gottstein, L. Neumann, H. Aretz, and R. Kopp: *Modell. Simul. Mater. Sci. Eng.*, 2004, vol. 12, pp. S1–18.
147. F. Roters, M. Diehl, P. Shanthraj, P. Eisenlohr, C. Reuber, S.L. Wong, T. Maiti, A. Ebrahimi, T. Hochrainer, H.-O. Fabritius, S. Nikolov, M. Friák, N. Fujita, N. Grilli, K.G.F. Janssens, N. Jia, P.J.J. Kok, D. Ma, F. Meier, E. Werner, M. Stricker, D. Weygand, and D. Raabe: *Comput. Mater. Sci.*, 2019, vol. 158, pp. 420–78.
148. A.D. Rollett: *Prog. Mater Sci.*, 1997, vol. 42, pp. 79–99.
149. H. Hallberg: *Metals*, 2011, vol. 1, pp. 16–48.
150. C. Schäfer, V. Mohles, and G. Gottstein: *Acta Mater.*, 2011, vol. 59, pp. 6574–87.